An optimal estimation based aerosol retrieval algorithm using OMI near-UV observations

Ukkyo Jeong[1], Jhoon Kim[1,*], Changwoo Ahn[2], Omar Torres[3], Xiong Liu[4], Pawan K. Bhartia[3], Robert J.D. Spurr[5], David Haffner[3], Kelly Chance[4], and Brent N. Holben[3]

[1]Dept. of Atmospheric Sciences, Yonsei University, Seoul, Korea

[2]Science Systems and Applications, Inc., Lanham, Maryland, USA

[3]Goddard Space Flight Center, NASA, Greenbelt, Maryland, USA

[4]Harvard-Smithsonian Center for Astrophysics, Cambridge, Massachusetts, USA

[5]RT Solutions, Inc., 9 Channing Street, Cambridge, Massachusetts, USA

*Corresponding author: Jhoon Kim (jkim2@yonsei.ac.kr)

Tel. +82-2-2123-5682, Fax. +82-2-365-5163

Abstract

An optimal estimation (OE) based aerosol retrieval algorithm using the OMI (Ozone Monitoring Instrument) near-ultraviolet observation was developed in this study. The OE-based algorithm has the merit of providing useful estimates of errors simultaneously with the inversion products. Furthermore, instead of using the traditional look-up tables for inversion, it performs online radiative transfer calculations with the Vector Linearized Discrete Ordinate Radiative Transfer (VLIDORT) model to eliminate interpolation errors and improve stability. The measurements and inversion products of the Distributed Regional Aerosol Gridded Observation Network campaign in Northeast Asia (DRAGON NE-Asia 2012) were used to validate the retrieved AOT and SSA. The retrieved AOT and SSA at 388 nm have a correlation with the Aerosol Robotic Network (AERONET) products that is comparable to or better than the correlation with the operational product during the campaign. The OE-based estimated error better represented the variance of actual biases of AOT at 388 nm between the retrieval and AERONET measurements than the operational error estimates. The forward model parameter errors were analyzed separately for both AOT and SSA retrievals. The surface reflectance at 388 nm, the imaginary part of the refractive index at 354 nm, and the number fine mode fraction (FMF) were found to be the most important parameters affecting the retrieval accuracy of AOT, while FMF was the most important parameter for the SSA retrieval. The additional information provided with the retrievals, including the estimated error and degrees of freedom, is expected to be valuable for relevant studies. Detailed advantages of using the OE method were described and discussed in this paper.

Key words

Aerosol; Error Analysis; Ozone Monitoring Instrument; Optimal Estimation Method; DRAGON campaign

1. Introduction

Anthropogenic aerosols have affected both the radiative and meteorological balance in the atmosphere and thus the radiative forcing of the atmosphere directly and indirectly (Ramanathan et al., 2001;Russell et al., 1999;Breon et al., 2002). To understand the role of aerosol in the atmosphere from a global perspective, reliable aerosol data from satellites are essential (Al-Saadi et al., 2005;Kinne et al., 2006). The several satellite-based aerosol retrieval methods based on multi-wavelength (Levy et al., 2007;Kim et al., 2007), multi-angle (Fisher et al., 2014), active light (Young et al., 2013), and polarization (Deuze et al., 2001) measurements have their own advantages and limitations. The inversion products from such measurements provide various parameters of aerosols at different channels. Thus, appropriate sources of aerosol information need to be employed for relevant studies.

An important advantage of using the ultraviolet (UV) channel to retrieve aerosol optical properties is that the results are less affected by uncertainties in surface reflectance (Torres et al., 1998). The retrieved aerosol products have relatively uniform quality over both land and ocean except over ice–snow surfaces (Torres et al., 2007;Herman et al., 1997). The near-UV technique for aerosol remote sensing has the additional merit of a long term data record including aerosol absorption properties of over 30 years starting from the launch of the Total Ozone Mapping Spectrometer (TOMS) on Nimbus-7 in 1978 (Torres et al., 1998;Torres et al., 2002a;Torres et al., 2005). Thus, the retrieved products using the near-UV technique from TOMS and Ozone Monitoring Instrument (OMI) measurements are appropriate for climatological research (Torres et al., 2002b;Torres et al., 2007). Information on aerosol extinction and absorption properties in the UV region is also important for estimating the air mass factor (AMF) for trace gas retrievals (Palmer et al., 2001;Lin et al., 2014). However, deriving information on aerosol using available hyperspectral measurements such as OMI and Global Ozone Monitoring Experiment (GOME) is quite challenging due to the relatively low spatial resolution compared to typical imagers. Thus, the

error estimates of retrievals using such sensors are particularly important to understand the reliability of the information, so that it can be used appropriately. The main objective of this study is to improve the applicability of the aerosol inversion products of OMI by providing the reliable error estimates of the retrievals.

Accuracy assessments of the retrieved aerosol optical properties using UV radiances have been performed by comparison with results from reference methods including ground, airborne, and satellite based remote sensing techniques (Torres et al., 2005;Jethva et al., 2014;Torres et al., 2002a;Ahn et al., 2014;Livingston et al., 2009;Ahn et al., 2008;Curier et al., 2008). The aerosol information content of selected OMI spectral radiances using a multi-wavelength algorithm has been estimated using principal component analysis for simulated radiances (Veihelmann et al., 2007). Uncertainty estimates of UV aerosol retrievals have also been calculated by perturbation analysis (Torres et al., 1998;Torres et al., 2002b). Inversion algorithms based on optimal estimation (OE) theory provide not only a constrained solution with respect to the *a priori* information but also detailed error analysis from well-categorized error sources (Rodgers, 2000). In addition, iterative inversion methods such as OE provide additional retrieval masking parameters (*e.g.*, cost function and convergence criteria). Recently developed OE-based retrieval methods have provided both improved inversion products and error estimates from the aerosol and surface error sources (Wagner et al., 2010;Govaerts et al., 2010;Wurl et al., 2010).

A large amount of aerosol is emitted from both natural and anthropogenic sources in East Asia (Lee et al., 2012). The spatial and temporal variations in aerosol optical properties are significant because of the diverse emission sources and trans-boundary transport (Jeong et al., 2011). Thus, the assumed aerosol inversion parameters may cause substantial uncertainties in the retrieval. However, there are insufficient ground-based measurements of aerosol optical properties with suitable spatial and temporal coverage in East Asia, despite their importance for global air quality and climate change. The Distributed Regional Aerosol Gridded Observation Network Northeast

Asia (DRAGON-NE Asia) 2012 campaign (http://aeronet.gsfc.nasa.gov/new_web/DRAGON-Asia_2012_Japan_South_Korea.html) provides valuable datasets including both urban and regional-scale observations at more than 40 sites in Northeast Asia. In the present study, an OE-based near-UV aerosol retrieval and error analysis algorithm is developed to provide both improved aerosol inversion products and estimates of their uncertainties. The retrieved aerosol products and estimated uncertainties are validated against the DRAGON-NE Asia 2012 campaign measurements.

2. Data

OMI is a nadir-viewing hyperspectral spectrometer aboard the EOS (Earth Observing System)-Aura spacecraft that measures upwelling radiances from the top of the atmosphere in the ultraviolet and visible (270–500 nm) regions with approximate spectral resolution of 0.5 nm (Levelt et al., 2006). The advantage of using OMI for aerosol retrieval is its higher spatial resolution than other UV hyperspectral spectrometers (from 13×24 km^2 at nadir to 28×150 km^2 at the swath extremes with median pixel size 15×32 km^2) together with its 2600-km-wide swath. The radiometric calibration procedure and the estimated accuracy of OMI are described in Dobber et al. (2006). To determine aerosol type and vertical distribution, the current OMI near-UV aerosol algorithm (OMAERUV) employs the Cloud–Aerosol Lidar with Orthogonal Polarization (CALIOP) monthly climatology of aerosol layer height and real-time Atmospheric Infrared Sounder (AIRS) carbon monoxide (CO) observations (Torres et al., 2013). Surface reflectances at 354 nm and 388 nm were assumed to be Lambertian and were taken from the TOMS climatology database. Aerosol vertical distribution and surface reflectance information identical to that used in the operational algorithm were used for the OE-based algorithm here.

In this study, the spatial and temporal domains for analysis were confined to the DRAGON-NE Asia 2012 campaign as shown in Figure 1 and Table 1. The gridded observation networks had high spatial resolution over the representative megacities in Northeast Asia: Seoul in South Korea

and Osaka in Japan. To validate and compare the retrieved aerosol products from OMI, level 2 campaign products were used from the aerosol robotic network (AERONET); 380 nm aerosol optical thickness (AOT) from direct sun measurements and spectral single scattering albedo (SSA) from almucantar inversion products (Holben et al., 1998;Dubovik and King, 2000;Dubovik et al., 2000;Dubovik et al., 2006). Retrieved 388 nm AOT from OMI was validated against AERONET 380 nm AOT. The OMI AOT retrievals within a radius of 0.5° of the AERONET site and within ±30 minutes of the OMI overpass time (about 13:40 local time) were averaged. The resulting OMI AOT average values were then compared with the time-averaged Sun photometer measurements.

Aerosol absorption properties are retrieved at different wavelengths by AERONET and OMI. The AERONET inversion products of the SSA are available at 440, 670, 860, and 1020 nm, while the OMAERUV algorithm retrieves the SSA at 354 nm and 388 nm. Earlier field studies found that aerosol absorption is a continuous function of wavelength in the ultraviolet to short infrared region (Kirchstetter et al., 2004;Russell et al., 2010). To compare the SSA values from OMI and AERONET at the same wavelength, the AERONET SSA at 388 nm was obtained by extrapolating the SSAs at 440–1020 nm using a spline function. Then the converted AERONET SSA at 388 nm was compared with the retrieved OMI SSA values even though uncertainties might exist in the transformation. Unlike the direct sun measurements including AOT, the inversion products of AERONET from almucantar measurements are retrieved less frequently and require appropriate atmospheric conditions for AOT (440 nm AOT > 0.4) and solar zenith angle (solar zenith angle > 45°) (Dubovik and King, 2000;Jethva et al., 2014). Such favorable atmospheric conditions for the inversion using almucantar measurements rarely overlap closely with the OMI overpass time. Furthermore, too narrow a time window around the satellite overpass time reduces the number of comparison samples. In this study, to secure enough data points the SSA of a region at OMI overpass time was assumed to adequately represent the daily values. For the comparison,

the converted 388 nm SSA from AERONET was averaged over a day and the OMI retrievals of 388 nm SSA were spatially averaged over a grid area of 0.5° × 0.5° centered on the AERONET site.

3. Method

3.1. Operational OMI near UV aerosol algorithm

The OMAERUV uses two channel radiances at 354 nm and 388 nm to estimate aerosol amount and absorption properties (Torres et al., 1998;Torres et al., 2007;Torres et al., 2013). AOT and SSA at 388 nm are retrieved from pre-calculated reflectance look-up tables (LUT) for pre-determined nodal points of observational geometry and aerosol optical properties, total optical depth, and aerosol layer height. Three major aerosol types are considered and listed in Table 2: desert dust, carbonaceous aerosols associated with biomass burning, and weakly absorbing sulfate-based aerosols (hereafter dust, smoke, and sulfate, respectively). Each aerosol type has an assumed particle size distribution (PSD) derived from the long-term statistics of AERONET inversion products. The UV real refractive index (n_r) is obtained from the Optical Properties Of Aerosols And Clouds (OPAC) database (Hess et al., 1998). In the operational algorithm, the imaginary refractive indices (n_i) at 354 nm are assumed to be 1.0, 1.2, and 1.4 times the retrieved n_i at 388 nm for sulfate, smoke, and dust aerosol, respectively (Torres et al., 2007;Jethva and Torres, 2011). The overall concept and design of the improved OMAERUV algorithm is well described by Torres et al. (2013).

There have been further improvements at updated OMAERUV (version 1.5.3), which was used for reprocessing the data of AOT and SSA in this study. The OMAERUV algorithm was refined by adjusting thresholds of UV aerosol index (UVAI) and Atmospheric Infrared Sounder (AIRS) CO data in determining aerosol types and retrieval approaches. A cloud screening scheme in assigning algorithm quality flags was also modified for retaining more good retrievals of carbonaceous and sulfate type aerosols when the CO level is high enough (higher than 3.2×10^{18} molecules·cm^{-2}) with various reflectivity thresholds. The UVAI threshold was changed from 0.8 to

0.5 over the oceans. This modification eliminates the land-ocean discontinuity in UVAI threshold. It is now identical (0.5) for both conditions. The current characterization of ocean reflective properties in the OMAERUV algorithm does not explicitly account for ocean color effects and, therefore, the quality of the retrieved aerosol properties over the oceans for low aerosol amounts would be highly uncertain. For that reason, retrievals over the oceans are only carried out for high concentrations of either desert dust or carbonaceous aerosols as indicated by UVAI values larger than or equal to 0.5.

Depending on the magnitude of the UVAI and CO parameters as well as the aerosol type, two retrieval approaches are currently used. They are referred to as two-channel and single-channel retrievals. In the two-channel approach, observations at 354 and 388 nm are used to simultaneously derive AOD and SSA. Over scenes when the aerosol absorption signal is low, the single-channel retrieval is applied. AOD is retrieved from the 388 nm observation assuming a value of 1.0 for SSA. Different CO threshold values are used for the northern and southern hemispheres to remove upper tropospheric CO which may not be necessarily associated with carbonaceous aerosols. A smoothing function in CO is used to transition from SH to NH threshold values. Specific criteria for retrieval approaches are summarized in Table 3. More detailed information of the latest update in OMAERUV is available from the Readme file at the web site (http://disc.sci.gsfc.nasa.gov/Aura/data-holdings/OMI/omaeruv_v003.shtml).

3.2. OE-based OMI near UV aerosol algorithm

The traditional LUT-based inversion method potentially includes errors due to interpolation between the nodal points and the local minimum, despite its high numerical efficiency. Such interpolation error typically depends on the interpolation method, number of the nodal points, and analytic characteristics of the parameters in LUT. In order to reduce the interpolation error, higher resolution of LUT nodal points is necessary which requires larger amount of numerical computation. Furthermore, in order to modify the retrieval algorithm, whole LUT should be re-calculated even

for a few number of target retrievals. The errors from the interpolation are also hard to evaluate as the LUT becomes more complicated.

On the contrary, online retrieval methods can reduce such errors from the interpolation and are numerically efficient particularly for the smaller number of target retrievals. Thus, online retrieval method is appropriate for the research purposes since retrieval sensitivity study typically use smaller number of sample compared to the operational purposes and prefer rapid and accurate results. In our experience, the online retrieval method was numerically more efficient compared to the LUT-based retrieval method by order of 1 or 2 for less than few thousands of retrievals. Furthermore, the online retrieval methods are optimized to avoid local minima by employing additional constraints to find more reliable and stable solutions (Kalman, 1960;Phillips, 1962;Tikhonov, 1963;Twomey, 1963;Chahine, 1968). However, employing online calculation as operational retrieval method requires large computation cost. Thus, using the online calculation as a benchmark results for the LUT-based algorithm is recommended to develop the optimized LUT for the operational purposes. Recent efforts to minimize the numerical cost of radiative transfer model and to increased calculation speed are expected to make the online calculation more practical even for the operational purposes.

Optimization for measurement error, the inclusion of *a priori* and ancillary data, and employing physical constraints (*e.g.,* non-negativity of measurements and retrievals) for an inversion method are important since each method has its own advantages and disadvantages (Dubovik, 2004). In this study, we used OE as the inversion method (Rodgers, 2000) since it has several advantages over other methods for OMI-like measurements, as discussed in Section 4. The atmospheric inverse problem often suffers from both insufficient information content of the measurements and imperfect measurement accuracy. Bayesian statistics provides mapping methods from the measurement probability density function (pdf) into state space with prior knowledge. Based on Bayes' theorem, the OE technique employs additional constraints from external sources (*a*

175 *priori*) to complement the insufficient information content of the measurements. For the nonlinear
176 inversion case, by considering the maximum *a posteriori* approach, the general form of the
177 Bayesian solution can be expressed as Equation (1) where measurement and *a priori* errors are
178 assumed to be Gaussian (Rodgers, 2000):
179
180 $$-2\ln P(\mathbf{x}|\mathbf{y}) = [\mathbf{y}-\mathbf{K}\mathbf{x}]^T\mathbf{S}_\epsilon^{-1}[\mathbf{y}-\mathbf{K}\mathbf{x}] + [\mathbf{x}-\mathbf{x}_a]^T\mathbf{S}_a^{-1}[\mathbf{x}-\mathbf{x}_a] + \mathbf{c} \quad (1)$$
181
182 where $\mathbf{x}$ is the state vector and $\mathbf{y}$ the measurement vector, $\mathbf{K}$ is the weighting function matrix,
183 $\mathbf{S}_\epsilon$ is the measurement error covariance matrix, $\mathbf{x}_a$ is the *a priori* mean state, and $\mathbf{S}_a$ is the *a*
184 *priori* covariance matrix. The formulation finds the optimized solution that minimizes the cost
185 function (χ):
186
$$\chi^2 = \left\|\mathbf{S}_\epsilon^{-\frac{1}{2}}(\mathbf{y}-\mathbf{K}\mathbf{x})\right\|_2^2 + \left\|\mathbf{S}_a^{-\frac{1}{2}}(\mathbf{x}-\mathbf{x}_a)\right\|_2^2 \quad (2)$$
187
188 Detailed derivations and implications are described in previous studies (Rodgers, 2000;Wurl et al.,
189 2010;Govaerts et al., 2010). As described above, the OMI near-UV algorithm uses radiance (I_{388})
190 and spectral contrast (I_{354}/I_{388}) for the measurement vector, where I_{354} and I_{388} are the
191 normalized radiances at 354 nm and 388 nm, respectively. The state vector in this study is the AOT
192 at 388 nm (τ_{388}) and the imaginary refractive index at 388 nm ($n_{i,388}$). Then, the weighting
193 function matrix can be expressed as follows:
194
$$\mathbf{K} = \begin{bmatrix} \dfrac{\partial I_{388}}{\partial \tau_{388}} & \dfrac{\partial I_{388}}{\partial n_{i,388}} \\ \dfrac{\partial}{\partial \tau_{388}}\left(\dfrac{I_{354}}{I_{388}}\right) & \dfrac{\partial}{\partial n_{i,388}}\left(\dfrac{I_{354}}{I_{388}}\right) \end{bmatrix} \quad (3)$$

where the weighting function of the spectral contrast can be obtained from the following derivative:

$$\frac{\partial}{\partial x}\left(\frac{I_{354}}{I_{388}}\right)=\frac{\frac{\partial I_{354}}{\partial x}I_{388}-I_{354}\frac{\partial I_{388}}{\partial x}}{(I_{388})^2} \tag{4}$$

In typical inversion methods, including OE, estimation of the reliable measurement error covariance matrix is important to determine the likelihood of the solution (Govaerts et al., 2010). The measurement error includes radiometric noise error and calibration accuracy. The absolute bidirectional scattering distribution function (BSDF) radiometric accuracy of the OMI instrument is reported to be about 4% for 2σ and the random noise error is provided in the level 1b product (Dobber et al., 2006). However, the reported BSDF uncertainty includes the errors in the calibration method and it represents whole wavelength domain. Thus, actual BSDF uncertainty at 354 and 388 nm would be less than 2% (Jaross, 2015). In our experience, 2% of BSDF uncertainty leads to the overestimates of the error and it is still challenging to evaluate. According to multiple retrieval tests, the BSDF uncertainty was assumed to be 1% in this study. The radiometric error covariance at each wavelength was calculated from the square root of the sum of squared radiometric uncertainty and calibration accuracy. The error covariance matrix can be written as:

$$\mathbf{S}_{\epsilon}=\begin{bmatrix}\sigma(\epsilon_{388})^2 & \sigma\left(\epsilon_{388},\epsilon_{354/388}\right)^2\\ \sigma\left(\epsilon_{388},\epsilon_{354/388}\right)^2 & \sigma\left(\epsilon_{354/388}\right)^2\end{bmatrix} \tag{5}$$

where ϵ_λ is the total error of the measured radiance at wavelength λ, $\epsilon_{354/388}$ is the error of I_{354}/I_{388}, which is described later in this section, and $\sigma(\epsilon_{388}, \epsilon_{354/388})^2$ is the covariance between the total measurement errors of I_{388} and I_{354}/I_{388}.

The ϵ_λ typically includes both random and systematic components and its covariance can be expressed as follows:

$$\sigma(\epsilon_\lambda)^2 = \sigma(\epsilon_{r,\lambda})^2 + \sigma(\epsilon_{s,\lambda})^2 \quad (6)$$

where $\epsilon_{r,\lambda}$ and $\epsilon_{s,\lambda}$ are the random and systematic components of radiometric error at λ, and $\sigma(\epsilon_{r,\lambda})^2$ and $\sigma(\epsilon_{s,\lambda})^2$ are their covariance values, respectively. The $\epsilon_{354/388}$ can be approximated as follows:

$$\epsilon_{354/388} \cong \frac{I_{354}}{I_{388}} - \frac{I_{354}+\epsilon_{354}}{I_{388}+\epsilon_{388}} \cong \frac{I_{354}}{I_{388}}\left(\frac{\epsilon_{354}}{I_{354}} - \frac{\epsilon_{388}}{I_{388}}\right) \cong \frac{I_{354}}{I_{388}}\left(\frac{\epsilon_{s,354}}{I_{354}} - \frac{\epsilon_{s,388}}{I_{388}} + \frac{\epsilon_{\mathrm{r},354}}{I_{354}} - \frac{\epsilon_{\mathrm{r},388}}{I_{388}}\right) \quad (7)$$

When the systematic components of the measurement errors of radiances at 354 nm and 388 nm are positively correlated and their values are similar, part of the systematic uncertainties can be reduced by the $\frac{\epsilon_{s,354}}{I_{354}} - \frac{\epsilon_{s,388}}{I_{388}}$ term. However, assessment of the systematic error of OMI measurements at each pixel is still challenging despite this partial reduction of systematic errors by using I_{354}/I_{388}. In this study, the BSDF calibration uncertainties of I_{354} and I_{388} at a pixel are assumed to be systematic and similar, while the radiometric noise values of I_{354} and I_{388} are assumed to be random and independent. Then, the systematic measurement error of $\epsilon_{354/388}$ can be regarded as negligible and the covariance of $\epsilon_{354/388}$ in Equation (7) can be approximated as follows:

$$\sigma\left(\epsilon_{354/388}\right) \cong \frac{I_{354}}{I_{388}}\sqrt{\left(\frac{\epsilon_{\mathrm{r},354}}{I_{354}}\right)^2 + \left(\frac{\epsilon_{\mathrm{r},388}}{I_{388}}\right)^2} \quad (8)$$

234

235 The $\sigma\left(\epsilon_{388}, \epsilon_{354/388}\right)^2$ can be obtained as follows:

236

$$\sigma\left(\epsilon_{388}, \epsilon_{354/388}\right)^2 = \frac{1}{n-1}\sum_{i=1}^{n} {\epsilon_{388}}^i {\epsilon_{354/388}}^i \quad (9)$$

237

238 where ${\epsilon_{388}}^i$ and ${\epsilon_{354/388}}^i$ are the uncertainties in the i^{th} measurement of I_{388} and I_{354}/I_{388} for
239 a sample of size *n*, respectively. Under the same assumptions used in Equations (7) and (8),
240 ${\epsilon_{354/388}}^i$ has only random and independent components, and so $\sigma\left(\epsilon_{388}, \epsilon_{354/388}\right)$ can be regarded
241 as negligible. The diagonal and off-diagonal elements of the measurement error covariance matrices
242 using two different measurement matrices are compared in Table 4.

243

244 **3.3. Error characterization**

245 Retrieved products with estimated and/or characterized error are valuable for any
246 application. Various error sources can be categorized as shown in the following equation by
247 linearizing the forward model with respect to associated parameters (Eyre, 1987;Rodgers, 1990,
248 2000):

249

$$\hat{\mathbf{x}} - \mathbf{x} = (\mathbf{A} - \mathbf{I}_n)(\mathbf{x} - \mathbf{x}_a) + \mathbf{G}_y\mathbf{K}_b\left(\mathbf{b} - \hat{\mathbf{b}}\right) + \mathbf{G}_y\Delta\mathbf{f}\left(\mathbf{x}, \mathbf{b}, \mathbf{b}^{'}\right) + \mathbf{G}_y\boldsymbol{\epsilon} \quad (10)$$

250

251 where $\hat{\mathbf{x}}$ and $\mathbf{x}$ are the retrieval and true states, respectively; $\mathbf{A}$ is the averaging kernel matrix; $\mathbf{I}_n$
252 is the identity matrix; $\mathbf{x}_a$ is the *a priori* state vector; $\mathbf{G}_y$ is the contribution function matrix; $\mathbf{K}_b$

is the weighting function matrix of forward model parameters (**b**); $\hat{\mathbf{b}}$ is the guessed forward model parameter; $\Delta\mathbf{f}$ is the error in the forward model relative to the real physics; and $\boldsymbol{\epsilon}$ is the measurement error. The first and last term on the right-hand-side (RHS) of Equation (10) is the smoothing error and retrieval noise, respectively. Their covariance matrices can be calculated from:

$$\mathbf{S}_s = (\mathbf{A} - \mathbf{I}_n)\mathbf{S}_E(\mathbf{A} - \mathbf{I}_n)^{\mathrm{T}} \tag{11}$$

$$\mathbf{S}_n = \mathbf{G}_y\mathbf{S}_\epsilon{\mathbf{G}_y}^{\mathrm{T}} \tag{12}$$

where $\mathbf{S}_s$ is the smoothing error covariance matrix, $\mathbf{S}_E$ is the covariance of the ensemble of states about the mean state, and $\mathbf{S}_n$ is the covariance matrix of the retrieval noise. We have assumed that the climatological value is a good representation of the real ensemble of the state about the mean state, and so the covariance matrix of the *a priori* state was employed as the $\mathbf{S}_E$ in this study. Each $\mathbf{S}_s$ and $\mathbf{S}_n$ has two diagonal elements that represent the variances of the smoothing error and retrieval noise for two retrievals, AOT and SSA. The smoothing error (ε_{sm}) and retrieval noise (ε_n) of AOT and SSA were defined as the square root of the corresponding diagonal elements of $\mathbf{S}_s$ and $\mathbf{S}_n$, respectively. The square root of the sum of squared ε_{sm} and ε_n of AOT and SSA are defined in this study as the solution errors (ε_{sol}) of AOT and SSA, respectively.

The second term on the RHS of Equation (10) is the forward model parameter error, and its covariance matrix can be calculated as follows:

$$\mathbf{S}_f = \mathbf{G}_y\mathbf{K}_b\mathbf{S}_b{\mathbf{K}_b}^{\mathrm{T}}{\mathbf{G}_y}^{\mathrm{T}} \tag{13}$$

where $\mathbf{S}_f$ is the covariance matrix of the forward model parameter error, and $\mathbf{S}_b$ is the error covariance matrix of forward model parameter, **b**. The forward model parameters of the near-UV method include the aerosol microphysical model parameters, aerosol vertical distribution,

meteorological profile (pressure and temperature), and surface properties. These forward model parameters contain both random and systematic components with different scales of spatial and temporal variation. Furthermore, each forward model parameter has a different uncertainty that is difficult to evaluate. In this study, $\mathbf{S}_f$ was analyzed separately with respect to each forward model parameter as suggested by Rodgers (2000). The forward model parameter error (ε_f) of AOT and SSA were obtained from the square root of the corresponding diagonal elements of each $\mathbf{S}_f$.

The third term on the RHS in Equation (10) is the forward model error that is caused by discrepancies between known and real physics. To simulate the earth-reflected radiance, VLIDORT (linearized pseudo-spherical vector discrete ordinate radiative transfer code, version 2.6) was used. This code is based on one of the most accurate radiative transfer solutions for a one-dimensional atmosphere (Spurr, 2006). Linearization of state vectors and forward model parameters are described in prior papers (Spurr et al., 2012;Spurr and Christi, 2014). Although the simulated radiances are expected to be accurate, the forward model error depends on factors including the number of streams, layers, and Legendre coefficients for the aerosol phase functions. To reduce the numerical errors that can arise from an insufficient number of coefficients, 3 Stokes parameters, 75 layers, 16 streams, and up to 500 Legendre coefficients for the aerosol phase matrix were used for the radiance simulations. However, it is still a challenge to evaluate other possible sources of forward model error such as Raman scattering and the three-dimensional effect of the atmosphere for retrieval. Such issues are beyond the scope of this study, and thus only smoothing error, retrieval noise, and forward model parameter error are evaluated here.

3.4. *A priori* characterization

Using reliable *a priori* information is important in the OE method since the final solutions are determined between the *a priori* state and the inversion space of a measurement. There are several sources of *a priori* information including climatological data, reliable measurements from

more accurate instruments, and calculations from models based on theoretical or empirical statistics (Govaerts et al., 2010;Wurl et al., 2010;Rodgers, 2000). Appropriate sources of *a priori* depend on the characteristics of the state vector and the accuracy of the *a priori* database. When the *a priori* state has a systematic bias away from the true state, this bias propagates to the retrieval products. In this study, 10 years (from 2005 to 2014) of OMAERUV 388 nm AOT and SSA in spring (from March to May) were used for the *a priori* data. Figure 2 shows the collected climatological data of the 388 nm AOT and SSA in East Asia used in this study. To avoid biases due to cloud contamination in the OMI products, averaged values and standard deviations (σ) with more than 70 data points were used.

4. Results

The dust event on 28th April 2012 has been selected to compare the aerosol optical properties from the operational product with the OE-based retrievals in this study. Figure 3 shows the true color image on that day from the Moderate Resolution Imaging Spectroradiometer (MODIS) Aqua and the UV aerosol index from OMI. To see the difference between the OE-based and operational algorithm in the same area, both methods were applied to measurements with an operational algorithm flag of 0, to avoid cloud contamination and radiometric calibration uncertainties. Some of the points retrieved by the operational algorithm were rejected in the OE-based retrievals when the cost function cut-off was applied, as described in this section.

The AOT and SSA at 388 nm from the operational and OE-based products are compared in Figure 4. The ε_{sol} of the retrieved AOT and SSA at 388 nm, degree of freedom, and χ are shown in Figure 5. The OE-based and operational AOT at 388 nm are similar, as shown in Figure 4 (a) and (b). Both products seem to be affected by snow and cloud contaminated pixels around Seoul in South Korea (37°N, 126°E), Tianjin in China (39°N, 116°E) and Nagano in Japan (36°N, 138°E). In Figure 5 (a), the ε_{sol} of retrieved AOT at 388 nm has relatively high values compared with the

AOT level at large viewing zenith angle. Noticeable discrepancies of SSA at 388 nm from the operational and OE-based products are evident in some of the areas as shown in Figure 4 (c) and (d). The operational algorithm performed single-channel retrieval around East Mongolia (47°N, 115°E), while the OE-based algorithm performed two-channel retrieval for all cases. Since this area has a low level of AOT, the information content of aerosol absorption property is insufficient, resulting in the low degrees of freedom shown in Figure 4 (b) and Figure 5 (c). Thus the OE-based SSA in this area (Figure 4 (d)) seems noisy and the ε_{sol} of SSA appears high. Similar results for the behavior of SSA are apparent around central Japan (38°N, 138°E). Thus, SSA values with high AOT and low ε_{sol} are recommended for the analysis, similar to the retrieval conditions for AERONET inversion products (Dubovik and King, 2000). Additional information provided on retrievals at each pixel in Figure 5 is expected to be valuable for relevant studies including trace gas retrieval and data assimilation.

Figure 6 shows the results of validation of operational and OE-based AOT retrievals at 388 nm. As shown in Figure 6 (a) and (b), the OE-based inversion method showed higher correlation coefficient (r = 0.82) and slightly improved slope (0.83) and offset (0.16) values than the operational algorithm (r = 0.71, slope = 0.71, and offset = 0.2). The Fisher's z-value between the correlation coefficients (Fisher, 1921) was 3.04 corresponding to two-tailed p-value of 0.0024. The Student's t-value for the difference between the two slopes is 2.10 with 512 degrees of freedom with the two-tailed p-value of 0.04. The statistical values show that difference between the two correlation coefficients and slopes are significant (p-value < 0.05). The Q values (percentage of AOT retrievals falling within an uncertainty envelope of ±30% or 0.1) of the OE-based retrievals and operational algorithm were similar (63.0%). When a measured radiance is affected by parameters that the theoretical radiative transfer model does not consider (*e.g.*, sub-pixel cloud contamination), the χ of the retrieval typically has a high value. In this study, retrievals with χ larger than a certain value (*i.e.*, 2.0 in this study) have been rejected. This limitation on retrievals imposed

by the χ reduced the number of retrievals with abnormally high biases, which might be associated with sub-pixel cloud contamination, in the operational algorithm in Figure 6 (a).

The SSA values at 388 nm from OMI operational products and OE-based inversion products were compared with those at 388 nm and 440 nm from AERONET inversion products as shown in Figure 7. The retrieved SSA at 388 nm from the operational algorithm showed comparable or higher values of $Q_{0.03}$ (59.2%) and $Q_{0.05}$ (85.1%) with those from the OE-based algorithm ($Q_{0.03}$ = 53.5%, $Q_{0.05}$ = 86.0%) when compared with the AERONET SSA at 440 nm (The $Q_{0.03}$ and $Q_{0.05}$ represent the percentage of SSA retrievals falling within an uncertainty envelope of ±0.03 and ±0.05, respectively). The retrieved 388 nm SSA from both the operational and OE-based algorithms showed similar correlation with the AERONET (r = 0.27 and 0.26 for operational and OE-based algorithms, respectively. Fisher's z-value is 0.1 with two-tailed p-value of 0.92). The retrieved SSA at 388 nm from the operational and OE-based algorithms showed slightly higher correlation with the converted 388 nm SSA from AERONET (r = 0.34 and 0.33 for the operational and OE-based algorithm, respectively) than with the 440 nm SSA from AERONET. However, the significances of the differences in r between converted and unconverted SSA comparisons were low (Fisher's z-values were 0.71 and 0.67 with two-tailed p-values of 0.48 and 0.50 for operational algorithm and OE-based algorithm, respectively). The retrieved SSA at 388 nm from the operational algorithm also showed comparable or higher values of $Q_{0.03}$ (59.2%) and $Q_{0.05}$ (83.9%) than those of the OE-based algorithm ($Q_{0.03}$ = 53.5%, $Q_{0.05}$ = 82.8%) when compared with converted SSA at 388 nm from AERONET.

The estimated retrieval uncertainties of the AOT at 388 nm from the operational algorithm (ε_{omi}, ±30% or 0.1) and estimated ε_{sol} were plotted against the biases relative to AERONET measurements as shown in Figure 8. The percentages of AOT retrieval biases from AERONET falling within the estimated retrieval errors of operational (Q_{omi}) and OE-based method (Q_{sol}) were 64.8% and 65.9%, respectively. The Q_{sol} was higher than Q_{omi} despite of the lower mean value of

375 ε_{sol} (0.20) than that of ε_{omi} (0.21). The error bars and black squares in Figure 8 represent the
376 moving σ and average value of the retrieval biases from AERONET as a function of estimated error,
377 respectively. As shown in Figure 8 (b), ε_{sol} better explained the moving σ of the actual biases
378 (r=0.93) than ε_{omi} in Figure 8 (a) (r=0.52). Fisher's z-value between the correlation coefficients
379 was 2.33 with two-tailed p-value of 0.02. The systematic biases of ε_{sol} and ε_{omi} (represented by
380 the moving average of each error estimates) are typically related to other error sources, including
381 forward model parameters and sub-pixel cloud contaminations. Since the ε_{sol} of retrieved AOT
382 considers the theoretical sensitivity of the retrieval biases to associated parameters, it explained the
383 retrieval uncertainties better than the ε_{omi}, which only considers the retrieved AOT values.

384 Table 5 shows the suggested error sources and their magnitudes from the OMI ATBD
385 (Algorithm Theoretical Basis Documents) (Torres et al., 2002b) and the values employed in this
386 study. Although the current OMI cloud masking method is based on long-term TOMS heritage,
387 there may still be ground pixels contaminated by sub-pixel clouds. As the TOA reflectance is
388 greatly increased by even a small amount of cloud, cloud contamination can cause large positive
389 biases in the AOT retrieval. Previous studies estimated the AOT retrieval errors due to 5% cloud
390 contamination to be of the order of 0.1 to 0.2 (Torres et al., 1998;Torres et al., 2002b). They also
391 reported an even higher error in the single scattering albedo (0 to 0.15) especially for strongly
392 absorbing aerosols. However, estimation of sub-pixel cloud contamination is difficult because of the
393 large spatio-temporal variability of clouds and the relatively large ground pixel size of OMI. Thus
394 the further error analysis of cloud contamination error budget from Torres et al. (2002b) was not
395 performed in this study. Typical uncertainties of the 354 nm and 388 nm surface reflectances were
396 assumed to be 0.01 for both land and ocean. The BSDF accuracy was assumed to be 1% (Dobber et
397 al., 2006;Jaross, 2015), and radiometric precision from OMI Level 1b data. To analyze the
398 uncertainty associated with the aerosol size information and refractive index, σ values of the size
399 parameter and n_r at 440 nm were taken from AERONET inversion products during the campaign

period. To analyze the assumed n_i at 354 nm, the $\mathbf{S}_b$ was also obtained from AERONET statistics during the campaign period. Aerosol vertical distribution is important as it affects aerosol retrieval using near-UV and blue channels, particularly for absorbing aerosols (Torres et al., 1998;de Graaf et al., 2005;Torres et al., 2013). However, accuracy assessments of the aerosol height information used are still challenging. Typical uncertainties of the assumed aerosol layer peak height and half width were assumed to be 2 km and 1 km, respectively, in this study. In the OE-based near-UV aerosol retrieval algorithm, all aerosols are assumed to be spherical and the optical properties are calculated from aerosol microphysical properties using the Mie solution. However, non-sphericity may cause significant uncertainties, especially for large particles (Mishchenko and Travis, 1994;Mishchenko et al., 1995;Mishchenko et al., 1997;Mishchenko et al., 2003;Dubovik et al., 2006), and aerosol morphology is quite complicated and requires further analysis for the near-UV region. This is out of the scope of this study and thus needs to be investigated in a future study. Therefore the uncertainties due to aerosol non-sphericity were not analyzed.

Figure 9 shows the average and σ values of ε_f of the retrieved AOT and SSA that were sampled for the validation in Figure 6 (b) and Figure 7 (b), (d). High values of ε_f for AOT appeared in n_i at 354 nm (0.34±0.25), surface reflectance at 388 nm (0.19±0.07), and the number fine mode fraction (FMF) (0.16±0.09). These values are higher or comparable with the mean ε_{sol} of retrieved AOT at 388 nm (0.20). Thus, the accuracy of AOT retrievals depends on not only the radiometric accuracy and information content but also the aerosol models and ancillary data of the surface reflectance, of which the effect is already well known. The FMFs of the sulfate (0.999596) and smoke type aerosols (0.999795) are similar while that for dust type aerosols is quite different (0.995650). Considering that the estimated σ value for FMF uncertainty in this study (0.0015, see Table 5) is much lower than the difference between the FMFs of dust type and other aerosols (~0.004, see Table 2), the errors resulting from selection of the wrong aerosol type can be more significant. The estimated ε_f of the surface reflectance at 388 nm was higher than the previously

suggested value (0.07–0.09 for AOT and <0.01 for SSA) in the OMI ATBD (Torres et al., 2002b). The ε_fs of AOT with respect to the surface reflectance at 354 nm (0.12±0.04), peak height of the aerosol vertical distribution (0.11±0.10), fine mode n_r (0.09±0.10), half width of the fine mode PSD (0.07±0.06), mean radius of the coarse mode PSD (0.06±0.03), and half width of the aerosol vertical distribution (0.06±0.05) showed similar moderate sensitivity. Those for the mean radius of the fine mode PSD (0.02±0.02) and half width of the coarse mode PSD (0.02±0.01) were smaller and that of the coarse mode n_r (0.003±0.004) was found to be negligible.

Among ε_fs of the SSA retrieval, the FMF error ($1.4\times10^{-2} \pm 6.4\times10^{-3}$) was the most important of the ε_fs of the SSA retrieval. Errors in n_i at 354 nm ($7.4\times10^{-3} \pm 2.8\times10^{-3}$) and the peak height of the aerosol vertical distribution ($5.2\times10^{-3} \pm 2.8\times10^{-3}$) were found to be the second most important. The ε_f of SSA with respect to the fine mode n_r ($3.9\times10^{-3} \pm 1.7\times10^{-3}$), width of the fine mode PSD ($3.8\times10^{-3} \pm 1.7\times10^{-3}$), the surface reflectance at 354 nm ($3.4\times10^{-3} \pm 1.8\times10^{-3}$) and 388 nm ($2.8\times10^{-3} \pm 2.1\times10^{-1}$), mean radius of the coarse mode PSD ($3.1\times10^{-3} \pm 1.1\times10^{-3}$), half width of the aerosol vertical distribution ($2.3\times10^{-3} \pm 1.5\times10^{-3}$), mean radius of the fine mode PSD ($1.1\times10^{-3} \pm 5.7\times10^{-4}$) and width of the coarse mode PSD ($8.7\times10^{-4} \pm 3.3\times10^{-4}$) were smaller and that of the coarse mode n_r ($5.2\times10^{-5} \pm 1.3\times10^{-4}$) appeared to be negligible. The estimated ε_fs of SSA were found to be about a factor magnitude lower than the ε_{sol} of SSA. The mean values of ε_{sm} and ε_n of SSA were 0.023 and 0.029, respectively. Thus, the estimated ε_{sol} of SSA at 388 nm is expected to be more reliable and represent the total uncertainties of SSA, since the uncertainty in SSA is predominantly affected by ε_{sol}, while uncertainty in AOT is affected by both ε_{sol} and ε_f. Note that the relative significances of the ε_fs of retrievals depend on their condition. It is additional merit of the error analysis using OE method that it provides specific error estimates of individual target event retrieval (*e.g.*, dust or biomass burning event). While analysis studies using satellite inversion products have often suffered from the statistic reliabilities, more reliable error estimates in this study are expected to contribute to the assessment of significances of the analysis.

5. Summary and Discussion

An OE-based aerosol retrieval and error characterization algorithm using the OMI near-UV radiances was developed in this study. The climatological values of OMAERUV products were employed as *a priori* data for the inversion method. The OE-based inversion method developed here provides not only the retrieved values of AOT and SSA but also estimates of their uncertainties. The retrieved AOT and SSA at 388 nm were compared with the AERONET products during the DRAGON-NE Asia 2012 campaign. The retrieved AOT using the OE method showed better results than the operational product. The OE-based SSA at 388 nm showed consistency with AERONET inversion products comparable to that of the operational SSA. The estimated retrieval noise and smoothing error of OE-based AOT represented well the variances of actual biases between the retrieved AOT and AERONET AOT. The forward model parameter errors were analyzed separately for both AOT and SSA inversion products. Uncertainties of surface reflectance at 388 nm, imaginary refractive index at 354 nm and number fine mode fraction were found to be the most important parameters affecting the retrieval accuracy of AOT, while uncertainties in the coarse mode real part of the refractive index had negligible effect. For SSA retrieval accuracy, number fine mode fraction was found to be the most important parameter while the other parameters appeared to have relatively small effects. As the FMF depends on the aerosol type, it is expected that more accurate aerosol type classification might improve the retrieval accuracy of AOT and SSA. For AOT retrieval, the estimated ε_f was comparable with the ε_{sol}, while the ε_f of SSA was negligible compared to the ε_{sol} of the retrieved SSA. It is also found that a sufficient amount of aerosol loading is necessary for reliable SSA retrieval.

However, there are still error sources which need to be analyzed, including the *a priori* error from climatology, aerosol morphology, cloud contamination, and three dimensional effects of radiative transfer. The assumed conditions in the inversion procedure also differ from the real state.

475 Validation studies for a longer period at more types of site are also necessary. Securing a more
476 reliable *a priori* database is expected to improve the OE-based aerosol retrieval algorithm.
477
478 **Acknowledgements**
479 This research was supported by the GEMS program of the Ministry of Environment, Korea and the
480 Eco Innovation Program of KEITI (2012000160002). The authors also acknowledge the KNMI and
481 NASA/GSFC for providing OMI and AERONET data.
482

References

Ahn, C., Torres, O., and Bhartia, P. K.: Comparison of ozone monitoring instrument UV aerosol products with Aqua/Moderate Resolution Imaging Spectroradiometer and Multiangle Imaging Spectroradiometer observations in 2006, J Geophys Res-Atmos, 113, Artn D16s27 Doi 10.1029/2007jd008832, 2008.

Ahn, C., Torres, O., and Jethva, H.: Assessment of OMI near-UV aerosol optical depth over land, J Geophys Res-Atmos, 119, 2457-2473, Doi 10.1002/2013jd020188, 2014.

Al-Saadi, J., Szykman, J., Pierce, R. B., Kittaka, C., Neil, D., Chu, D. A., Remer, L., Gumley, L., Prins, E., Weinstock, L., MacDonald, C., Wayland, R., Dimmick, F., and Fishman, J.: Improving national air quality forecasts with satellite aerosol observations, B Am Meteorol Soc, 86, 1249-+, Doi 10.1175/Bams-86-9-1249, 2005.

Breon, F. M., Tanre, D., and Generoso, S.: Aerosol effect on cloud droplet size monitored from satellite, Science, 295, 834-838, DOI 10.1126/science.1066434, 2002.

Chahine, M. T.: Determination of temperature profile in an atmosphere from its outgoing radiance, J. Opt. Soc. Am., 12, 1634-1637, 1968.

Curier, R. L., Veefkind, J. P., Braak, R., Veihelmann, B., Torres, O., and de Leeuw, G.: Retrieval of aerosol optical properties from OMI radiances using a multiwavelength algorithm: Application to western Europe, J Geophys Res-Atmos, 113, Artn D17s90 Doi 10.1029/2007jd008738, 2008.

de Graaf, M., Stammes, P., Torres, O., and Koelemeijer, R. B. A.: Absorbing Aerosol Index: Sensitivity analysis, application to GOME and comparison with TOMS, J Geophys Res-Atmos, 110, Artn D01201 Doi 10.1029/2004jd005178, 2005.

Deuze, J. L., Breon, F. M., Devaux, C., Goloub, P., Herman, M., Lafrance, B., Maignan, F., Marchand, A., Nadal, F., Perry, G., and Tanre, D.: Remote sensing of aerosols over land surfaces from POLDER-ADEOS-1 polarized measurements, J Geophys Res-Atmos, 106,

4913-4926, Doi 10.1029/2000jd900364, 2001.

Dobber, M. R., Dirksen, R. J., Levelt, P. F., Van den Oord, G. H. J., Voors, R. H. M., Kleipool, Q., Jaross, G., Kowalewski, M., Hilsenrath, E., Leppelmeier, G. W., de Vries, J., Dierssen, W., and Rozemeijer, N. C.: Ozone-Monitoring Instrument calibration, Ieee T Geosci Remote, 44, 1209-1238, Doi 10.1109/Tgrs.2006.869987, 2006.

Dubovik, O., and King, M. D.: A flexible inversion algorithm for retrieval of aerosol optical properties from Sun and sky radiance measurements, J Geophys Res-Atmos, 105, 20673-20696, Doi 10.1029/2000jd900282, 2000.

Dubovik, O., Smirnov, A., Holben, B. N., King, M. D., Kaufman, Y. J., Eck, T. F., and Slutsker, I.: Accuracy assessments of aerosol optical properties retrieved from Aerosol Robotic Network (AERONET) Sun and sky radiance measurements, J Geophys Res-Atmos, 105, 9791-9806, Doi 10.1029/2000jd900040, 2000.

Dubovik, O.: Optimization of numerical inversion in photopolarimetic remote sensing, Photopolarimetry in Remote Sensing, 65-106, 2004.

Dubovik, O., Sinyuk, A., Lapyonok, T., Holben, B. N., Mishchenko, M., Yang, P., Eck, T. F., Volten, H., Munoz, O., Veihelmann, B., van der Zande, W. J., Leon, J. F., Sorokin, M., and Slutsker, I.: Application of spheroid models to account for aerosol particle nonsphericity in remote sensing of desert dust, J Geophys Res-Atmos, 111, Artn D11208 Doi 10.1029/2005jd006619, 2006.

Eyre, J. R.: On Systematic-Errors in Satellite Sounding Products and Their Climatological Mean-Values, Q J Roy Meteor Soc, 113, 279-292, Doi 10.1256/Smsqj.47515, 1987.

Fisher: On the "probable error" of a coefficient of correlation deduced from a small sample, Metron, 1, 3-32, 1921.

Fisher, D., Muller, J. P., and Yershov, V. N.: Automated Stereo Retrieval of Smoke Plume Injection Heights and Retrieval of Smoke Plume Masks From AATSR and Their Assessment With

533 CALIPSO and MISR, Ieee T Geosci Remote, 52, 1249-1258, Doi 10.1109/Tgrs.2013.2249073,
534 2014.
535 Govaerts, Y. M., Wagner, S., Lattanzio, A., and Watts, P.: Joint retrieval of surface reflectance and
536 aerosol optical depth from MSG/SEVIRI observations with an optimal estimation approach: 1.
537 Theory, J Geophys Res-Atmos, 115, Artn D02203 Doi 10.1029/2009jd011779, 2010.
538 Herman, J. R., Bhartia, P. K., Torres, O., Hsu, C., Seftor, C., and Celarier, E.: Global distribution of
539 UV-absorbing aerosols from Nimbus 7/TOMS data, J Geophys Res-Atmos, 102, 16911-16922,
540 Doi 10.1029/96jd03680, 1997.
541 Hess, M., Koepke, P., and Schult, I.: Optical properties of aerosols and clouds: The software
542 package OPAC, B Am Meteorol Soc, 79, 831-844, Doi 10.1175/1520-
543 0477(1998)079<0831:Opoaac>2.0.Co;2, 1998.
544 Holben, B. N., Eck, T. F., Slutsker, I., Tanre, D., Buis, J. P., Setzer, A., Vermote, E., Reagan, J. A.,
545 Kaufman, Y. J., Nakajima, T., Lavenu, F., Jankowiak, I., and Smirnov, A.: AERONET - A
546 federated instrument network and data archive for aerosol characterization, Remote Sens
547 Environ, 66, 1-16, Doi 10.1016/S0034-4257(98)00031-5, 1998.
548 Jaross, G.: disccusion of OMI BSDF calibration accuracy, in, edited by: Jeong, U., SSAI, Lanham,
549 Maryland, USA, 2015.
550 Jeong, U., Kim, J., Lee, H., Jung, J., Kim, Y. J., Song, C. H., and Koo, J. H.: Estimation of the
551 contributions of long range transported aerosol in East Asia to carbonaceous aerosol and PM
552 concentrations in Seoul, Korea using highly time resolved measurements: a PSCF model
553 approach, J Environ Monitor, 13, 1905-1918, Doi 10.1039/C0em00659a, 2011.
554 Jethva, H., and Torres, O.: Satellite-based evidence of wavelength-dependent aerosol absorption in
555 biomass burning smoke inferred from Ozone Monitoring Instrument, Atmos Chem Phys, 11,
556 10541-10551, DOI 10.5194/acp-11-10541-2011, 2011.
557 Jethva, H., Torres, O., and Ahn, C.: Global assessment of OMI aerosol single-scattering albedo

using ground-based AERONET inversion, J Geophys Res-Atmos, 119, 9020-9040, Doi 10.1002/2014jd021672, 2014.

Kalman, R. E.: A new approach to linear filtering and prediction problems, Journal of Basic Engineering, 82, 35-45, 1960.

Kim, J., Lee, J., Lee, H. C., Higurashi, A., Takemura, T., and Song, C. H.: Consistency of the aerosol type classification from satellite remote sensing during the Atmospheric Brown Cloud-East Asia Regional Experiment campaign, J Geophys Res-Atmos, 112, Artn D22s33 Doi 10.1029/2006jd008201, 2007.

Kinne, S., Schulz, M., Textor, C., Guibert, S., Balkanski, Y., Bauer, S. E., Berntsen, T., Berglen, T. F., Boucher, O., Chin, M., Collins, W., Dentener, F., Diehl, T., Easter, R., Feichter, J., Fillmore, D., Ghan, S., Ginoux, P., Gong, S., Grini, A., Hendricks, J. E., Herzog, M., Horowitz, L., Isaksen, I., Iversen, T., Kirkavag, A., Kloster, S., Koch, D., Kristjansson, J. E., Krol, M., Lauer, A., Lamarque, J. F., Lesins, G., Liu, X., Lohmann, U., Montanaro, V., Myhre, G., Penner, J. E., Pitari, G., Reddy, S., Seland, O., Stier, P., Takemura, T., and Tie, X.: An AeroCom initial assessment - optical properties in aerosol component modules of global models, Atmos Chem Phys, 6, 1815-1834, 2006.

Kirchstetter, T. W., Novakov, T., and Hobbs, P. V.: Evidence that the spectral dependence of light absorption by aerosols is affected by organic carbon, J Geophys Res-Atmos, 109, Artn D21208 Doi 10.1029/2004jd004999, 2004.

Lee, J., Kim, J., Yang, P., and Hsu, N. C.: Improvement of aerosol optical depth retrieval from MODIS spectral reflectance over the global ocean using new aerosol models archived from AERONET inversion data and tri-axial ellipsoidal dust database, Atmos Chem Phys, 12, 7087-7102, DOI 10.5194/acp-12-7087-2012, 2012.

Levelt, P. F., Van den Oord, G. H. J., Dobber, M. R., Malkki, A., Visser, H., de Vries, J., Stammes, P., Lundell, J. O. V., and Saari, H.: The Ozone Monitoring Instrument, Ieee T Geosci Remote,

583 44, 1093-1101, Doi 10.1109/Tgrs.2006.872333, 2006.
584 Levy, R. C., Remer, L. A., Mattoo, S., Vermote, E. F., and Kaufman, Y. J.: Second-generation
585 operational algorithm: Retrieval of aerosol properties over land from inversion of Moderate
586 Resolution Imaging Spectroradiometer spectral reflectance, J Geophys Res-Atmos, 112, Artn
587 D13211 Doi 10.1029/2006jd007811, 2007.
588 Lin, J. T., Martin, R. V., Boersma, K. F., Sneep, M., Stammes, P., Spurr, R., Wang, P., Van
589 Roozendael, M., Clemer, K., and Irie, H.: Retrieving tropospheric nitrogen dioxide from the
590 Ozone Monitoring Instrument: effects of aerosols, surface reflectance anisotropy, and vertical
591 profile of nitrogen dioxide, Atmos Chem Phys, 14, 1441-1461, DOI 10.5194/acp-14-1441-
592 2014, 2014.
593 Livingston, J. M., Redemann, J., Russell, P. B., Torres, O., Veihelmann, B., Veefkind, P., Braak, R.,
594 Smirnov, A., Remer, L., Bergstrom, R. W., Coddington, O., Schmidt, K. S., Pilewskie, P.,
595 Johnson, R., and Zhang, Q.: Comparison of aerosol optical depths from the Ozone Monitoring
596 Instrument (OMI) on Aura with results from airborne sunphotometry, other space and ground
597 measurements during MILAGRO/INTEX-B, Atmos Chem Phys, 9, 6743-6765, 2009.
598 Mishchenko, M. I., and Travis, L. D.: T-Matrix Computations of Light-Scattering by Large
599 Spheroidal Particles, Opt Commun, 109, 16-21, Doi 10.1016/0030-4018(94)90731-5, 1994.
600 Mishchenko, M. I., Lacis, A. A., Carlson, B. E., and Travis, L. D.: Nonsphericity of Dust-Like
601 Tropospheric Aerosols - Implications for Aerosol Remote-Sensing and Climate Modeling,
602 Geophys Res Lett, 22, 1077-1080, Doi 10.1029/95gl00798, 1995.
603 Mishchenko, M. I., Travis, L. D., Kahn, R. A., and West, R. A.: Modeling phase functions for
604 dustlike tropospheric aerosols using a shape mixture of randomly oriented polydisperse
605 spheroids, J Geophys Res-Atmos, 102, 16831-16847, Doi 10.1029/96jd02110, 1997.
606 Mishchenko, M. I., Geogdzhayev, I. V., Liu, L., Ogren, J. A., Lacis, A. A., Rossow, W. B.,
607 Hovenier, J. W., Volten, H., and Munoz, O.: Aerosol retrievals from AVHRR radiances:

effects of particle nonsphericity and absorption and an updated long-term global climatology of aerosol properties, J Quant Spectrosc Ra, 79, 953-972, Doi 10.1016/S0022-4073(02)00331-X, 2003.

Palmer, P. I., Jacob, D. J., Chance, K., Martin, R. V., Spurr, R. J. D., Kurosu, T. P., Bey, I., Yantosca, R., Fiore, A., and Li, Q. B.: Air mass factor formulation for spectroscopic measurements from satellites: Application to formaldehyde retrievals from the Global Ozone Monitoring Experiment, J Geophys Res-Atmos, 106, 14539-14550, Doi 10.1029/2000jd900772, 2001.

Phillips, B. L.: A technique for numerical solution of certain intergral equation of first kind, Journal of Assoc. Comput. Mach., 9, 84-97, 1962.

Ramanathan, V., Crutzen, P. J., Kiehl, J. T., and Rosenfeld, D.: Atmosphere - Aerosols, climate, and the hydrological cycle, Science, 294, 2119-2124, DOI 10.1126/science.1064034, 2001.

Rodgers, C. D.: Characterization and Error Analysis of Profiles Retrieved from Remote Sounding Measurements, J Geophys Res-Atmos, 95, 5587-5595, Doi 10.1029/Jd095id05p05587, 1990.

Rodgers, C. D.: Inverse method for atmospheric sounding: theory and practice, World Scientific Publishing Co. Pte. Ltd., Singapore, 2000.

Russell, P. B., Hobbs, P. V., and Stowe, L. L.: Aerosol properties and radiative effects in the United States East Coast haze plume: An overview of the Tropospheric Aerosol Radiative Forcing Observational Experiment (TARFOX), J Geophys Res-Atmos, 104, 2213-2222, Doi 10.1029/1998jd200028, 1999.

Russell, P. B., Bergstrom, R. W., Shinozuka, Y., Clarke, A. D., DeCarlo, P. F., Jimenez, J. L., Livingston, J. M., Redemann, J., Dubovik, O., and Strawa, A.: Absorption Angstrom Exponent in AERONET and related data as an indicator of aerosol composition, Atmos Chem Phys, 10, 1155-1169, 2010.

Spurr, R., Wang, J., Zeng, J., and Mishchenko, M. I.: Linearized T-matrix and Mie scattering

computations, J Quant Spectrosc Ra, 113, 425-439, 10.1016/j.jqsrt.2011.11.014, 2012.

Spurr, R., and Christi, M.: On the generation of atmospheric property Jacobians from the (V)LIDORT linearized radiative transfer models, J Quant Spectrosc Ra, 142, 109-115, 10.1016/j.jqsrt.2014.03.011, 2014.

Spurr, R. J. D.: VLIDORT: A linearized pseudo-spherical vector discrete ordinate radiative transfer code for forward model and retrieval studies in multilayer multiple scattering media, J Quant Spectrosc Ra, 102, 316-342, DOI 10.1016/j.jqsrt.2006.05.005, 2006.

Tikhonov, A. N.: On the solution of incorrectly stated problems and a method of regularization, Dokl. Akad. Nauk., 151, 501-504, 1963.

Torres, O., Bhartia, P. K., Herman, J. R., Ahmad, Z., and Gleason, J.: Derivation of aerosol properties from satellite measurements of backscattered ultraviolet radiation: Theoretical basis (vol 103, pg 17099, 1998), J Geophys Res-Atmos, 103, 23321-23321, 1998.

Torres, O., Bhartia, P. K., Herman, J. R., Sinyuk, A., Ginoux, P., and Holben, B.: A long-term record of aerosol optical depth from TOMS observations and comparison to AERONET measurements, J Atmos Sci, 59, 398-413, Doi 10.1175/1520-0469(2002)059<0398:Altroa>2.0.Co;2, 2002a.

Torres, O., Decae, R., Veefkind, J. P., and de Leeuw, G.: OMI aerosol retrieval algorithm, in OMI Algorithm Theoretical Basis Document, NASA Goddard Space Flight Cent., Greenbelt, Md., USA, 47-71, 2002b.

Torres, O., Bhartia, P. K., Sinyuk, A., Welton, E. J., and Holben, B.: Total Ozone Mapping Spectrometer measurements of aerosol absorption from space: Comparison to SAFARI 2000 ground-based observations, J Geophys Res-Atmos, 110, Artn D10s18 Doi 10.1029/Jd004611, 2005.

Torres, O., Tanskanen, A., Veihelmann, B., Ahn, C., Braak, R., Bhartia, P. K., Veefkind, P., and Levelt, P.: Aerosols and surface UV products from Ozone Monitoring Instrument observations:

658 An overview, J Geophys Res-Atmos, 112, Artn D24s47 Doi 10.1029/2007jd008809, 2007.
659 Torres, O., Ahn, C., and Chen, Z.: Improvements to the OMI near-UV aerosol algorithm using A-
660 train CALIOP and AIRS observations, Atmos Meas Tech, 6, 3257-3270, DOI 10.5194/amt-6-
661 3257-2013, 2013.
662 Twomey, S.: On the numerical solution of Fredholm integral equations of the first kind by the
663 inversion of the linear system produced by quadrature, Journal of Assoc. Comput. Mach., 10,
664 97-101, 1963.
665 Veihelmann, B., Levelt, P. F., Stammes, P., and Veefkind, J. P.: Simulation study of the aerosol
666 information content in OMI spectral reflectance measurements, Atmos Chem Phys, 7, 3115-
667 3127, 2007.
668 Wagner, S. C., Govaerts, Y. M., and Lattanzio, A.: Joint retrieval of surface reflectance and aerosol
669 optical depth from MSG/SEVIRI observations with an optimal estimation approach: 2.
670 Implementation and evaluation, J Geophys Res-Atmos, 115, Artn D02204 Doi
671 10.1029/2009jd011780, 2010.
672 Wurl, D., Grainger, R. G., McDonald, A. J., and Deshler, T.: Optimal estimation retrieval of aerosol
673 microphysical properties from SAGE II satellite observations in the volcanically unperturbed
674 lower stratosphere, Atmos Chem Phys, 10, 4295-4317, DOI 10.5194/acp-10-4295-2010, 2010.
675 Young, S. A., Vaughan, M. A., Kuehn, R. E., and Winker, D. M.: The Retrieval of Profiles of
676 Particulate Extinction from Cloud-Aerosol Lidar and Infrared Pathfinder Satellite Observations
677 (CALIPSO) Data: Uncertainty and Error Sensitivity Analyses, J Atmos Ocean Tech, 30, 395-
678 428, Doi 10.1175/Jtech-D-12-00046.1, 2013.
679

Tables and Figures

Table captions

Table 1. Positions and mean AOT and SSA at 388 nm of the AERONET sites during the DRAGON-NE Asia 2012 campaign.

Table 2. Aerosol number-size distribution parameters* and real refractive index (n_r) for each aerosol type in the OMI near-UV algorithm.

Table 3. Retrieval approach criteria of OMI near-UV algorithm version 1.5.3.

Table 4. Diagonal and off-diagonal elements of the measurement error covariance matrices using two different measurement matrices.

Table 5. Error sources and their assumed magnitudes in the OMI ATBD (Algorithm Theoretical Basis Documents) and this study.

693 **List of tables**

694 **Table 1.** Positions and mean AOT and SSA at 388 nm of the AERONET sites during the
695 DRAGON-NE Asia 2012 campaign.

Site name	Latitude (°) (North)	Longitude (°) (East)	Mean 380 nm AOT	Mean 440 nm SSA
Baengnyeong	37.97	124.63	0.56	0.96
Yonsei Univ., Seoul	37.56	126.94	0.63	0.93
Anmyeon	36.54	126.33	0.57	0.94
Bokjeong, Seoul	37.46	127.13	0.75	0.90
Gangneung Wonju National Univ.	37.77	128.87	0.53	0.92
Guwol, Seoul	37.45	126.72	0.69	0.94
GIST, Gwangju	35.23	126.84	0.54	0.93
HUFS, Yongin	37.34	127.27	0.63	0.90
Kongju National Univ., Kongju	36.47	127.14	0.62	0.96
Konkuk Univ., Seoul	37.54	127.08	0.67	0.92
Korea Univ., Seoul	37.59	127.03	0.73	0.92
Kunsan National Univ., Kunsan	35.94	126.68	0.61	0.92
Kyungil Univ., Kyungsan	36.07	128.82	0.57	0.93
Mokpo National Univ., Mokpo	34.91	126.44	0.58	0.93
NIER, Incheon	37.57	126.64	0.62	0.93
Pusan National Univ., Pusan	35.24	129.08	0.62	0.93
Sanggye, Seoul	37.66	127.07	0.73	0.92
Sinjeong, Seoul	37.52	126.86	0.64	0.91
Soha, Seoul	37.45	126.89	0.69	0.91
Gosan, Jeju	33.29	126.16	0.62	0.96
Seoul National Univ., Seoul	37.46	126.95	0.65	0.93
Fukuoka	33.52	130.48	0.50	0.90
Kohriyama	37.36	140.38	0.34	0.95
Kyoto	35.03	135.78	0.47	0.94
Matsue	35.48	133.01	0.56	0.93
Mt. Ikoma	34.68	135.68	0.39	0.96
Mt. Rokko	34.76	135.23	0.41	0.95
Nara	34.69	135.83	0.48	0.94
Nishiharima	35.03	134.34	0.42	0.95
North Osaka	34.77	135.51	0.52	0.94
South Osaka	34.54	135.50	0.55	0.94

Tsukuba	36.05	140.12	0.38	0.94
Noto	37.33	137.14	0.41	0.94
Shirahama	33.69	135.36	0.41	0.96
Chiba University	35.63	140.10	0.31	0.92
Fukue	32.75	128.68	0.78	0.92

700 **Table 2.** Aerosol number-size distribution parameters* and real refractive index (n_r) for each aerosol
701 type in the OMI near-UV algorithm.

Aerosol Model	r_g m1 [μm]	r_g m2 [μm]	σ m1 [μm]	σ m2 [μm]	FMF	n_r	$n_{i,354/388}$
Sulfate	0.088	0.509	1.499	2.160	0.999596	1.40	1.0
Smoke	0.080	0.705	1.492	2.075	0.999795	1.50	1.2
Dust	0.052	0.670	1.697	1.806	0.995650	1.55	1.4

702 *Number-weighted particle size distribution parameters: fine and coarse mode radii (r_g m1 and r_g
703 m2) and variance (σ m1 and σ m2), number fine mode fraction (FMF).
704
705
706
707 **Table 3.** Retrieval approach criteria of OMI near-UV algorithm version 1.5.3.

Surface Category	UVAI	CO (10^{18} molecules-cm^{-2})	Surface Type	Aerosol Type	Retrieval Approach
Ocean	≥ 0.5	> 2.2 NH (1.8 SH)	N/A*	Smoke	Two-channel
Ocean	≥ 0.5	≤ 2.2 NH (1.8 SH)	N/A	Dust	Two-channel
Ocean	< 0.5	-	-	-	No retrieval
Land	≥ 0.5	> 2.2 NH (1.8 SH)	All	Smoke	Two-channel
Land	≥ 0.5	≤ 2.2 NH (1.8 SH)	All	Dust	Two-channel
Land	< 0.5	>2.2 NH (1.8 SH)	All	Sulfate	Two-channel
Land	< 0.5	≤ 2.2 NH (1.8 SH)	All but arid	Sulfate	Single channel
Land	< 0.5	≤ 2.2 NH (1.8 SH)	arid	Dust	Single Channel

708 *Not available.
709

710 **Table 4.** Diagonal and off-diagonal elements of the measurement error covariance matrices using
711 two different measurement matrices.

Measurement matrix	$[I_{354}\ \ I_{388}]^T$	$\left[I_{354}\ \ \frac{I_{354}}{I_{388}}\right]^T$
First diagonal term	$\sigma(\epsilon_{354})^2$	$\sigma(\epsilon_{388})^2$
Second diagonal term	$\sigma(\epsilon_{388})^2$	$\left(\frac{I_{354}}{I_{388}}\right)^2\left\{\left(\frac{\epsilon_{r,354}}{I_{354}}\right)^2+\left(\frac{\epsilon_{r,388}}{I_{388}}\right)^2\right\}$
Off-diagonal term	$\sigma(\epsilon_{354},\epsilon_{388})^2$	0

712

713 **Table 5.** Error sources and their assumed magnitudes in the OMI ATBD (Algorithm Theoretical
714 Basis Documents) and this study.

Error source	Error perturbation (OMI ATBD)	Assumed value of σ for each error source in this study
Cloud Contamination	5% cloud contamination	NA[+]
Surface Reflectivity	0.01 error in surface reflectivity	0.01 for both wavelengths
Radiometric uncertainty	SNR less than 1%	1% of BSDF calibration uncertainty (Dobber et al., 2006; Jaross, 2015)
	Radiometric offset additive error of 1%	
	Radiometric scale factor multiplicative error of 1%	Radiometric precision provided by Level 1b data
Size distribution (mode radius)	5% increase of mode radius	0.019 for fine mode[*]
		0.510 for coarse mode[*]
Size distribution (width)	5% increase of width	0.265 for fine mode[*]
		0.307 for coarse mode[*]
Fine mode fraction	NA	0.0015[*]
Refractive index	Increase with 0.05 for n_r	0.053 for n_r (for all wavelengths and size modes)[*]
	Increase with 0.01 for n_i	0.0047 for 354 nm n_i[*]
Aerosol Vertical Profile	Change of 1 km peak height	Change of 2 km peak height
		Change of 1 km half width
Particle shape	NA	NA

715 [*]Standard deviation of each parameter during the DRAGON-NE Asia 2012 campaign. The
716 parameters for n_r and n_i were obtained from 440 nm AERONET inversion products.
717 [+]Not analyzed.

718 **Figure captions**

719 **Figure 1.** Mean 380 nm aerosol optical thickness (AOT) and 440 nm single scattering albedo and
720 their probability density functions during the DRAGON-NE Asia 2012 campaign.

721 **Figure 2.** (a) Mean and (b) standard deviation of 388 nm AOT from the OMAERUV product in
722 spring (March to May) 2005–2014. Panels (c) and (d) show the average and standard deviation of
723 SSA, respectively, during the same period.

724 **Figure 3.** (a) MODIS Aqua true color image and (b) UV aerosol index from the OMI product in
725 Northeast Asia on 28th April 2012.

726 **Figure 4.** (a) OMI operational AOT, (b) OE-based AOT, (c) operational SSA, and (d) OE-based
727 SSA on 28th April 2012 at 388 nm.

728 **Figure 5.** Estimated S_{sn} of (a) OE-based 388 nm AOT and (b) SSA. Panels (c) and (d) show the
729 degrees of freedom and cost function of the retrieval, respectively.

730 **Figure 6.** Validation of 388 nm AOT against AERONET data from (a) operational products and (b)
731 the OE-based algorithm during the DRAGON-NE Asia 2012 campaign.

732 **Figure 7.** Comparison of the 440 nm SSA from AERONET and 388 nm SSA from (a) the
733 operational products and (b) the OE-based algorithm, during the DRAGON-NE Asia 2012
734 campaign. Panels (c) and (d) compare converted 388 nm SSA from AERONET with that from (c)
735 the operational products and (d) the OE-based algorithm.

736 **Figure 8.** Comparison between estimated uncertainties of the 388 nm AOT (*x*-axis) and biases of
737 retrieved AOT from AERONET measurements (*y*-axis). The panels (a) and (b) are based on the
738 operational and OE-based retrieval/error-estimation algorithm, respectively.

739 **Figure 9.** Average (gray bars) and standard deviation (black lines) of the forward model parameter
740 errors of 388 nm (a) AOT and (b) SSA.

741

742

List of figures

[Figure 1]

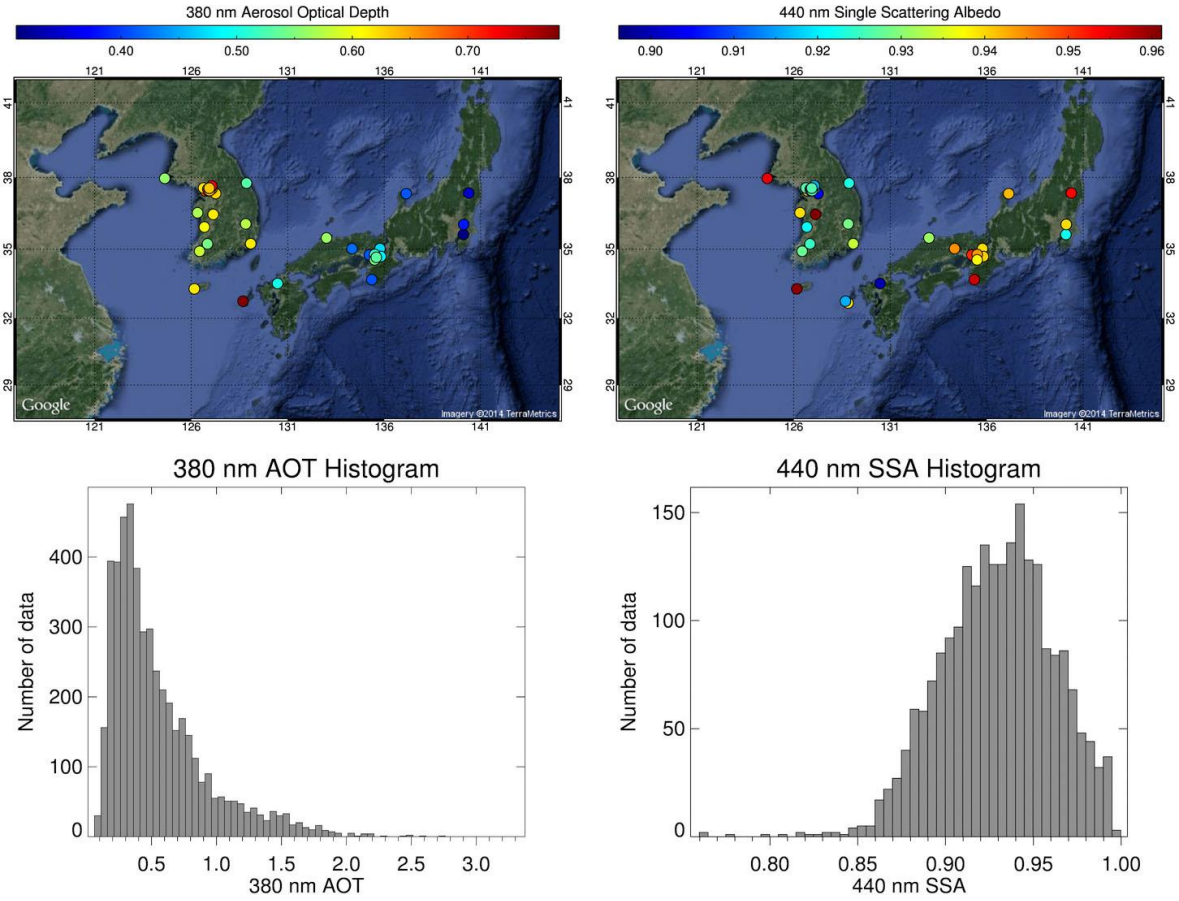

Figure 1. Mean 380 nm aerosol optical thickness (AOT) and 440 nm single scattering albedo and their probability density functions during the DRAGON-NE Asia 2012 campaign.

[Figure 2]

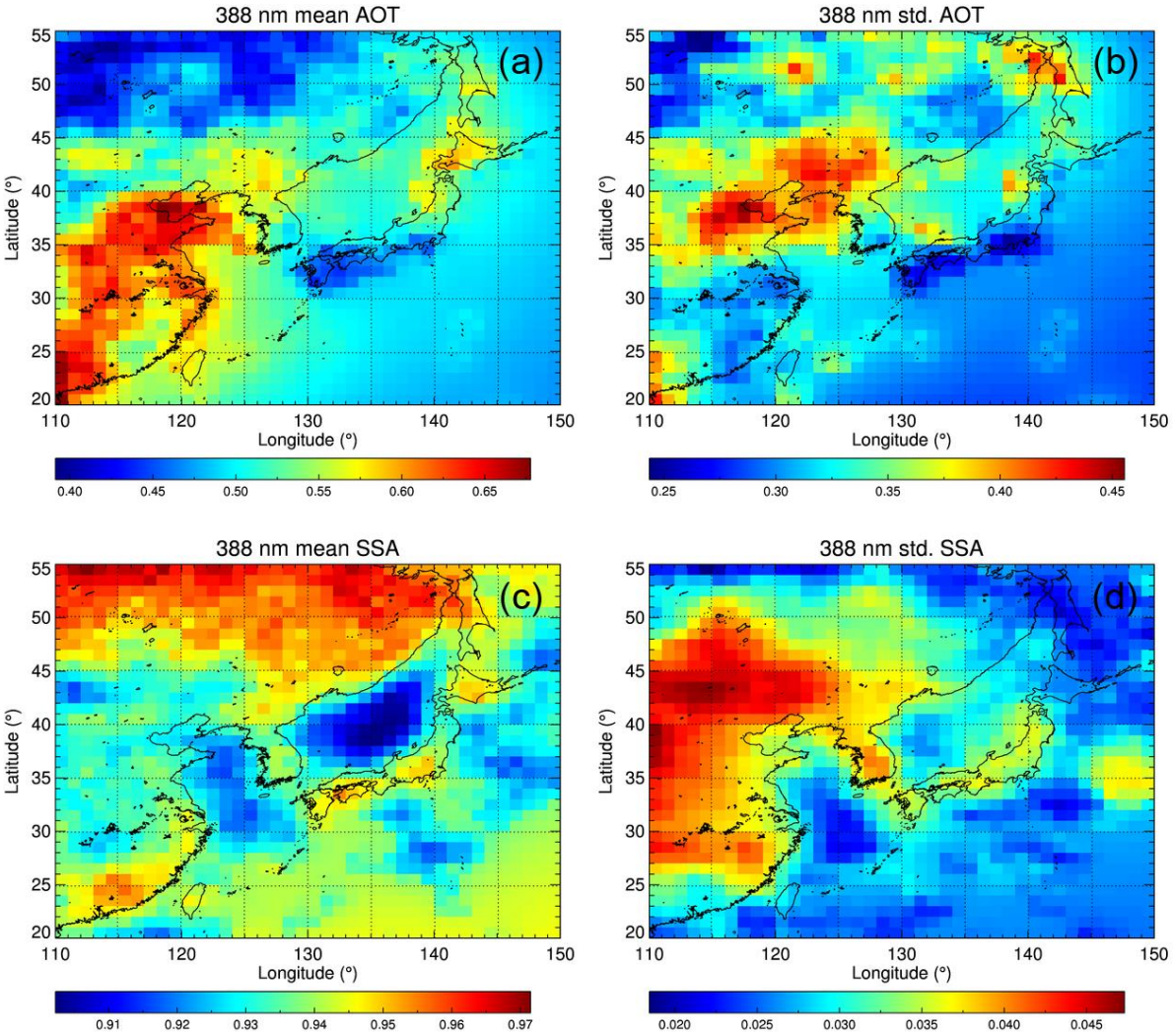

Figure 2. (a) Mean and (b) standard deviation of 388 nm AOT from the OMAERUV product in spring (March to May) 2005–2014. Panels (c) and (d) show the average and standard deviation of SSA, respectively, during the same period.

[Figure 3]

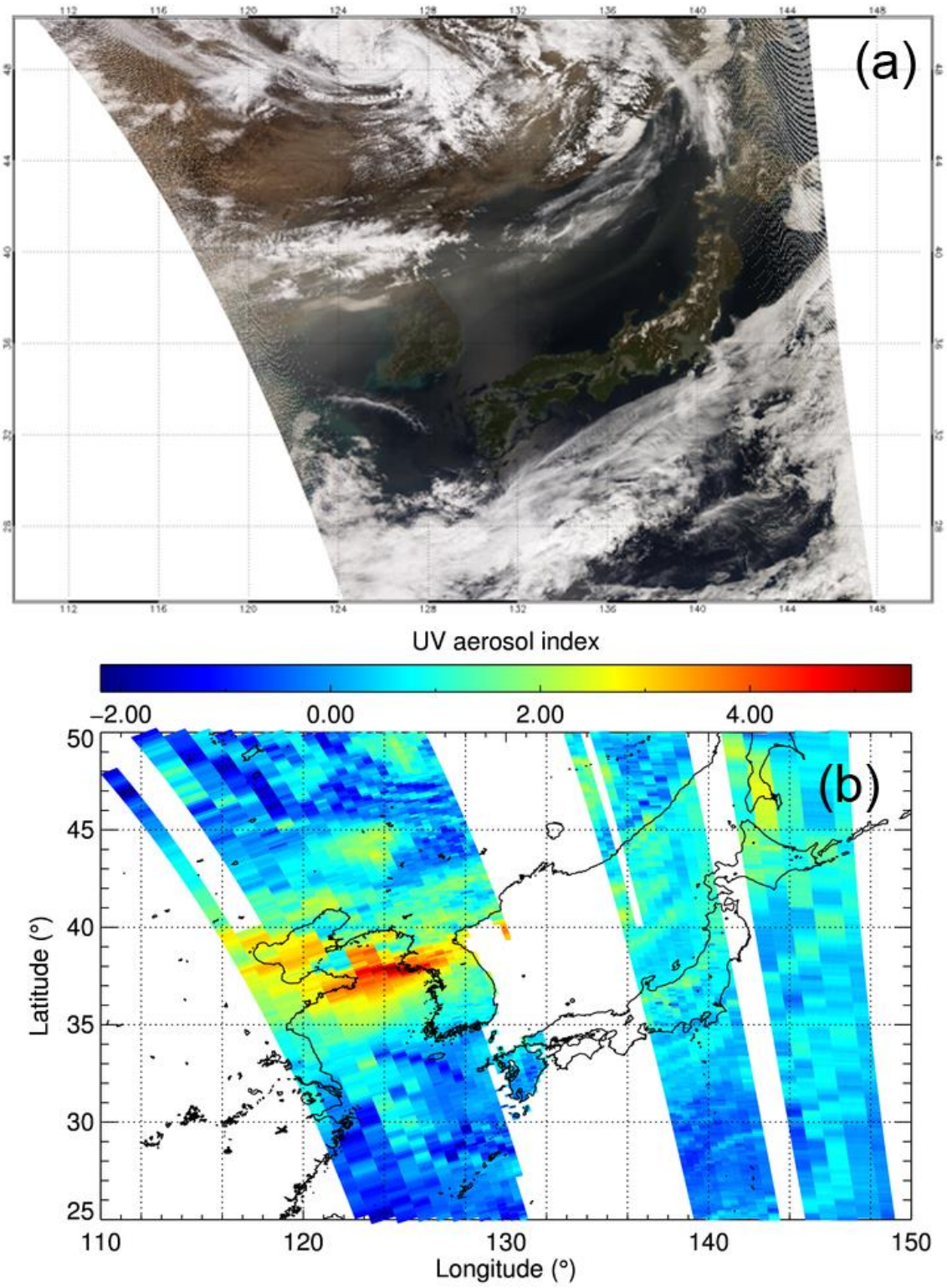

Figure 3. (a) MODIS Aqua true color image and (b) UV aerosol index from the OMI product in Northeast Asia on 28th April 2012.

760 **[Figure 4]**

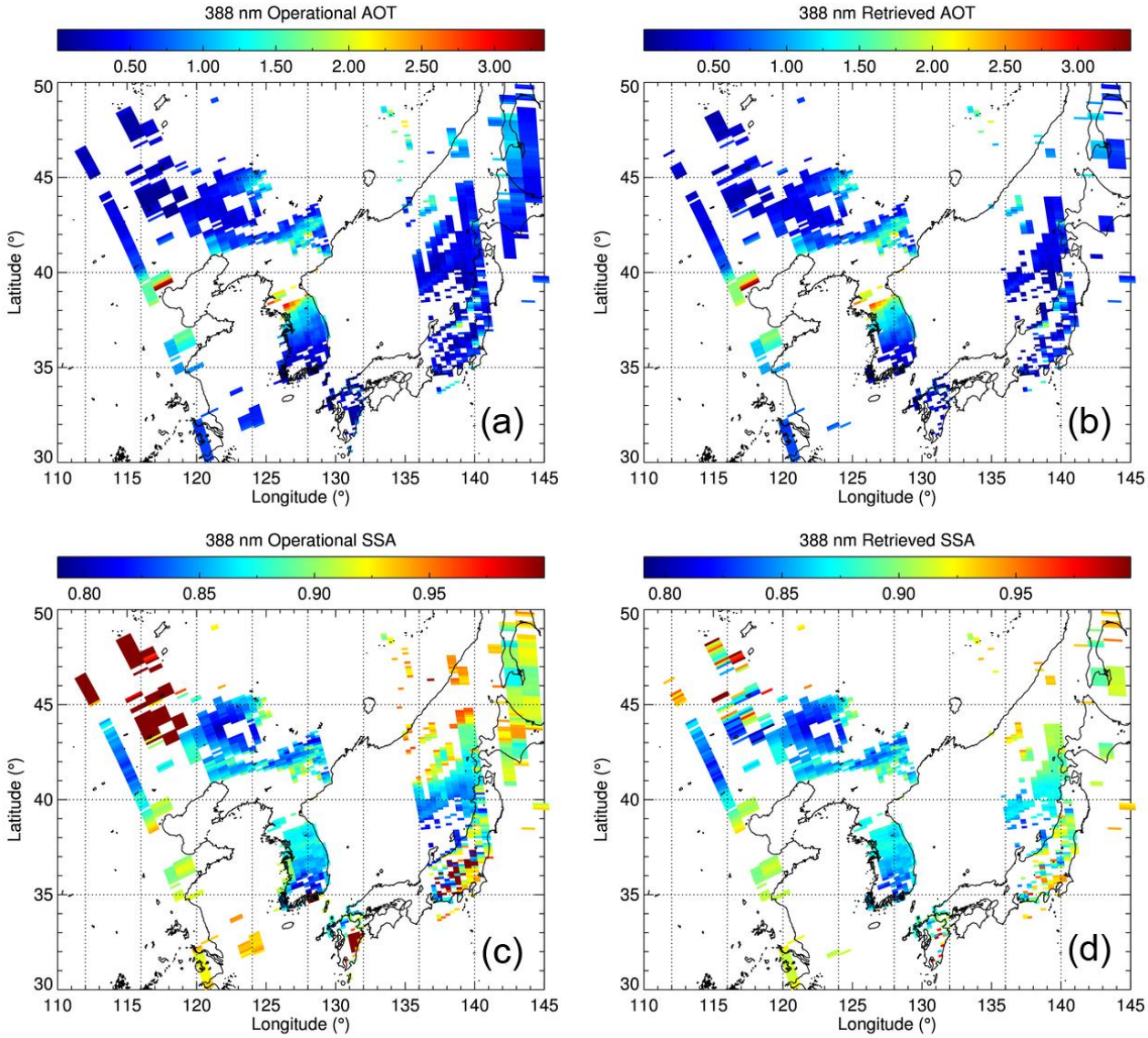

761

762 **Figure 4.** (a) OMI operational AOT, (b) OE-based AOT, (c) operational SSA, and (d) OE-based

763 SSA on 28th April 2012 at 388 nm.

764 **[Figure 5]**

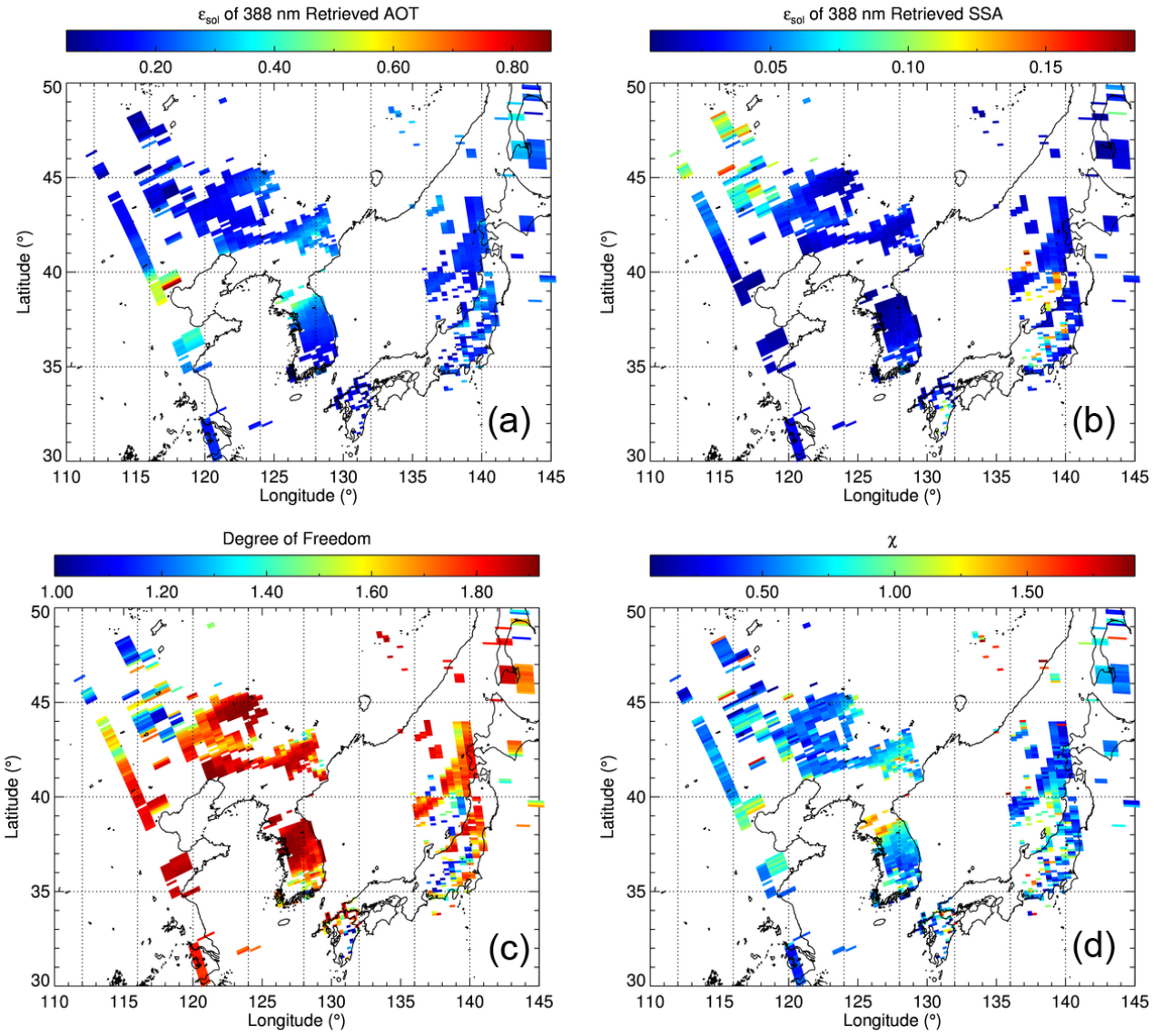

765

766 **Figure 5.** Estimated solution error of (a) OE-based 388 nm AOT and (b) SSA. Panels (c) and (d)

767 show the degrees of freedom and cost function of the retrieval, respectively.

768

769 **[Figure 6]**

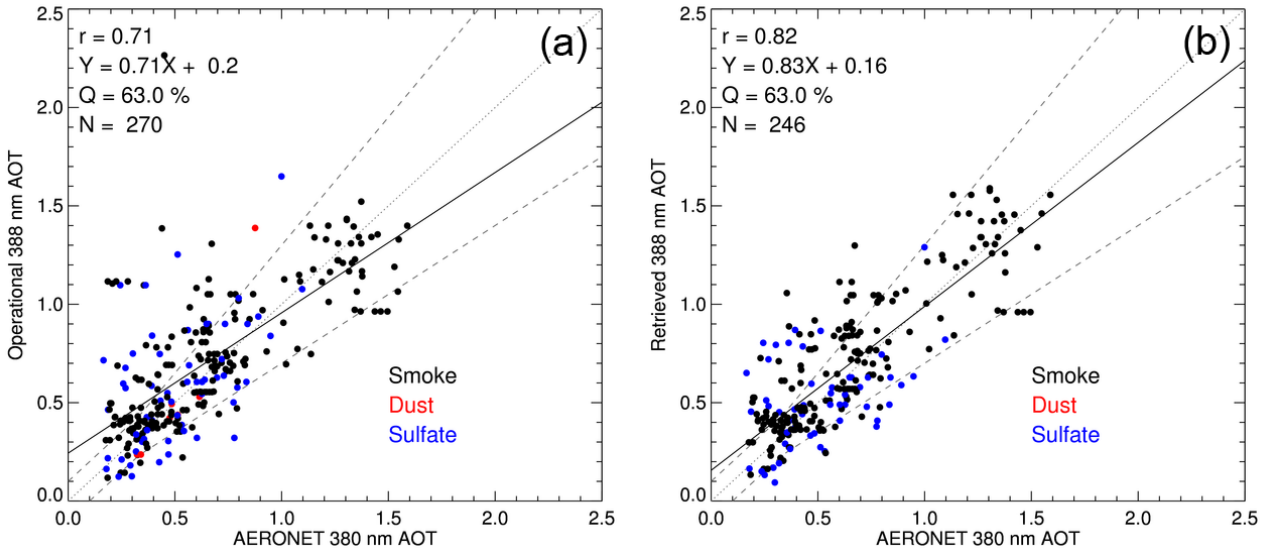

770

771 **Figure 6.** Validation of 388 nm AOT against AERONET data from (a) operational products and (b)

772 the OE-based algorithm during the DRAGON-NE Asia 2012 campaign.

773

774 **[Figure 7]**

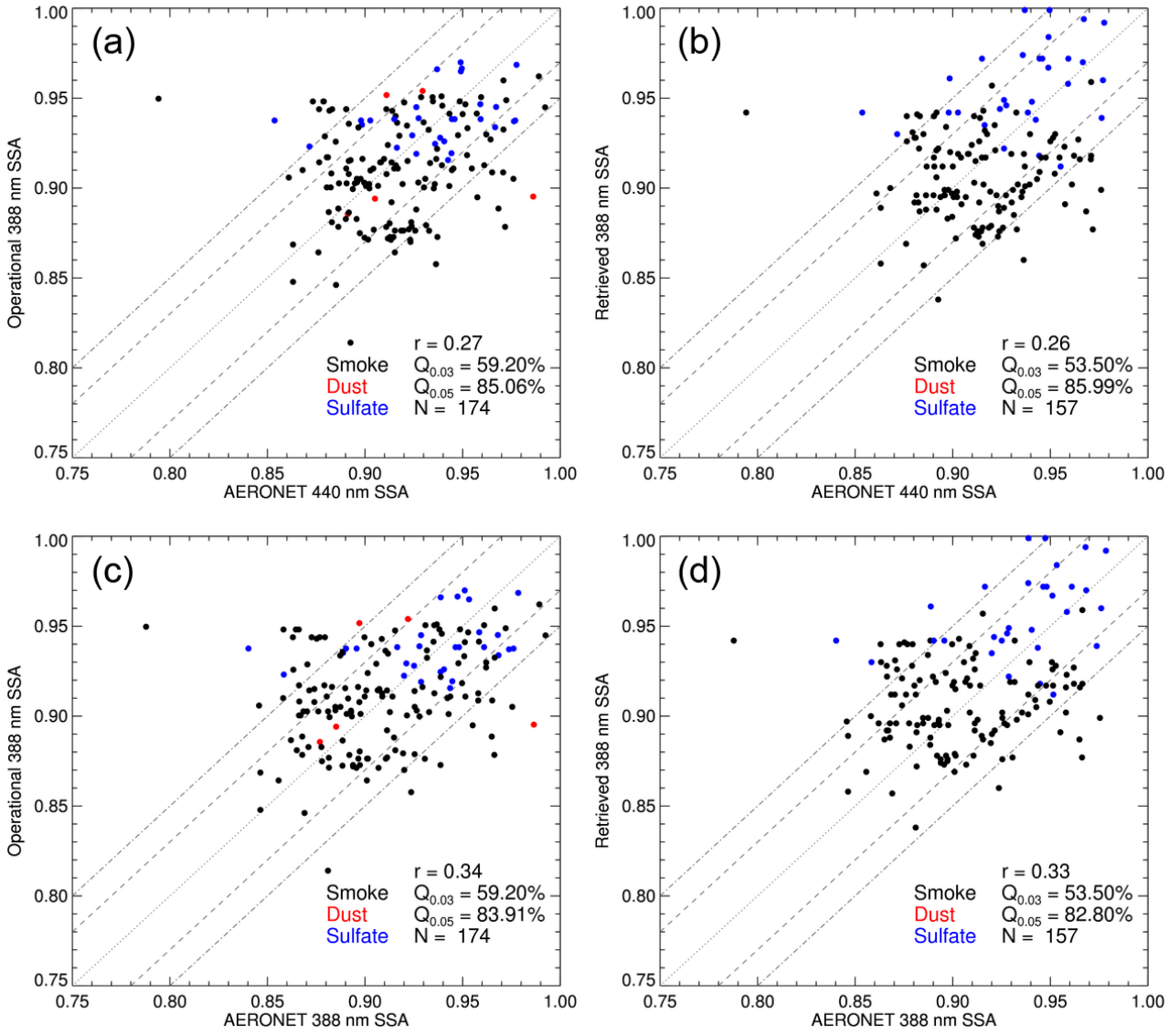

775

776 **Figure 7.** Comparison of the 440 nm SSA from AERONET and 388 nm SSA from (a) the
777 operational products and (b) the OE-based algorithm, during the DRAGON-NE Asia 2012
778 campaign. Panels (c) and (d) compare converted 388 nm SSA from AERONET with that from (c)
779 the operational products and (d) the OE-based algorithm.

780

781 **[Figure 8]**

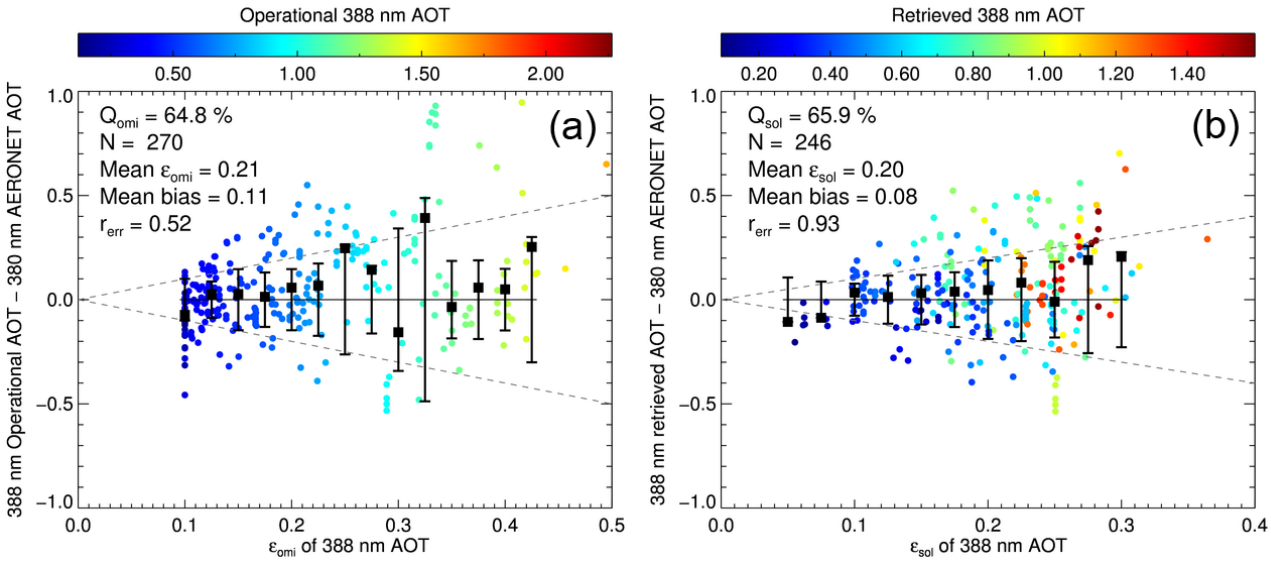

782

783 **Figure 8.** Comparison between estimated uncertainties of the 388 nm AOT (*x*-axis) and biases of
784 retrieved AOT from AERONET measurements (*y*-axis). The panels (a) and (b) are based on the
785 operational and OE-based retrieval/error-estimation algorithm, respectively.

786

787 **[Figure 9]**

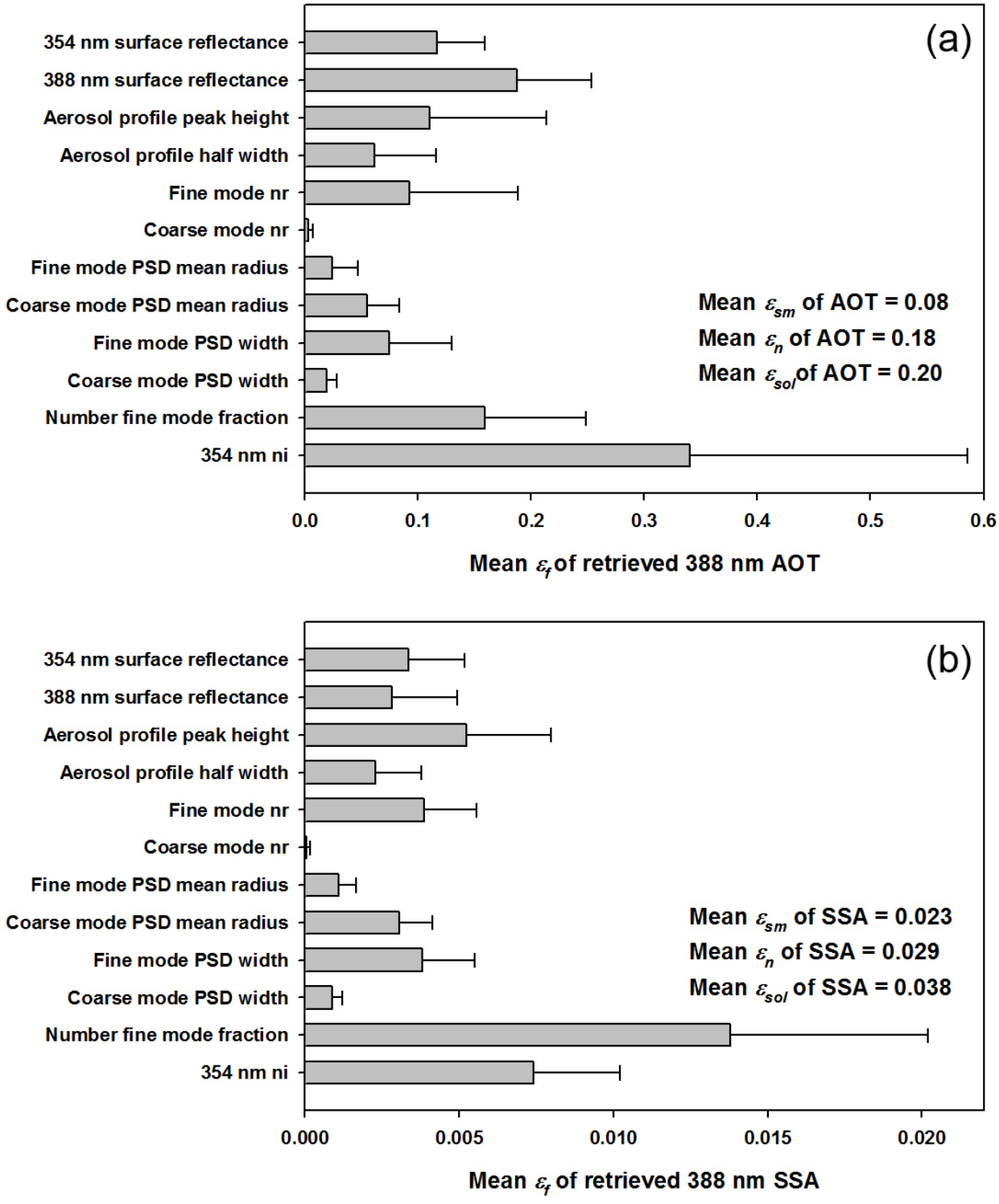

788

789 **Figure 9.** Average (gray bars) and standard deviation (black lines) of the forward model parameter

790 errors of 388 nm (a) AOT and (b) SSA.